Advances in Robotics Research, *Vol. 1, No. 3 (2014) 215-237*
DOI: http://dx.doi.org/10.12989/arr.2014.1.3.215

Haptic feedback from human tissues of various stiffness and homogeneity

Neil Vaughan[1a], Venketesh N. Dubey[*1], Michael Y. K. Wee[2] and Richard Isaacs[2]

[1]*Bournemouth University, Faculty of Science and Technology, Poole, BH12 5BB, United Kingdom*
[2]*Poole Hospital NHS Foundation Trust, Longfleet Road, Poole, BH15 2JB, United Kingdom*

(Received September 17, 2014, Revised January 5, 2015, Accepted January 12, 2015)

Abstract. This work presents methods for haptic modelling of soft and hard tissue with varying stiffness. The model provides visualization of deformation and calculates force feedback during simulated epidural needle insertion. A spring-mass-damper (SMD) network is configured from magnetic resonance image (MRI) slices of patient's lumbar region to represent varying stiffness throughout tissue structure. Reaction force is calculated from the SMD network and a haptic device is configured to produce a needle insertion simulation. The user can feel the changing forces as the needle is inserted through tissue layers and ligaments. Methods for calculating the force feedback at various depths of needle insertion are presented. Voxelization is used to fill ligament surface meshes with spring mass damper assemblies for simulated needle insertion into soft and hard tissues. Modelled vertebrae cannot be pierced by the needle. Graphs were produced during simulated needle insertions to compare the applied force to haptic reaction force. Preliminary saline pressure measurements during Tuohy epidural needle insertion are also used as a basis for forces generated in the simulation.

Keywords: soft tissue; tissue model; haptic feedback; human tissue model; medical simulation

1. Introduction

During surgically invasive procedures, tissues deform under the forces and influence of surgical instruments, changing the shapes of the volumetric tissue regions by stretching or compressing. This has effect on water vessels in the surrounding area, and the shapes of volumetric tissue regions. It also affects the density and elasticity of the tissue. These affect the path of surgical implements. In the case of epidural insertion, training simulators attempt to model the path of the needle which needs to take into account deformation. Advanced medical simulations need to model anatomically correct tissue deformation by modelling physical interaction between each anatomical structure and the functional nature of human organs.

Haptic devices are being increasingly incorporated into medical training, and this has become a rapidly growing area of research in biomedical simulations. Medical simulators are similar to flight simulators for pilots, allowing trainees to learn and practice difficult procedures in a risk-free

*Corresponding author, Associate Professor, E-mail: vdubey@bmth.ac.uk
[a]Postdoctoral Researcher, E-mail: nvaughan@bmth.ac.uk

http://www.techno-press.org/?journal=arr&subpage=7 ISSN: 2287-4976 (Print), 2287-4984 (Online)

virtual environment engaging several senses with auditory, visual and haptic feedback. Haptic techniques have been applied to several medical procedures including needle insertion (DiMaio *et al*. 2002), bone dissection (Agus *et al*. 2003), laparoscopy and suturing (Panait *et al*. 2009). Haptic epidural needle insertion simulators have been developed (Manoharan *et al*. 2012) but not based on measured data, giving lower accuracy. The capabilities of haptic models such as spring-mass-damper (SMD) to represent tissue deformation and reaction forces have not been fully explored.

This research includes a data collection trial (Vaughan *et al*. 2012) to take measurements from needle insertions in porcine cadaver and with obstetric patients to determine the actual forces involved. The aim is to apply haptic techniques to simulate epidural needle insertion. Epidural Tuohy needle insertion is an ideal procedure for haptic simulation, since the epiduralist presses the needle through several tissue layers, each having a different feeling and force feedback. During the in-vivo procedure, the feeling provides the main indication of current needle position when it pierces skin, subcutaneous fat, Supraspinous and interspinous ligaments, ligamentum flavum and then into the epidural space with the "loss of resistance". These could be represented by haptic modelling of soft and hard materials. In-vivo the operator cannot see needle position so they use sense of touch.

Haptic simulations apply collision detection between the needle and the tissue, and then calculate resulting interaction forces. With needles, reaction force from the interaction with tissue not only occurs at their extremity but also along their length. This reaction force is comprised of many factors including friction, cutting force, stiffness and to name a few.

Okamura *et al*. (2004) developed a force model for needle insertion based on data from bovine liver tissue, reporting that bevel tip causes more needle bending and is more easily affected by tissue density variations than triangular and diamond tips. Forces for larger diameter needles measured higher due to increased cutting and friction forces.

Recently magnetic resonance elastography (MRE) has demonstrated suitability for non-invasive mapping of mechanical properties of tissue including elasticity, stiffness and temperature (Kruse *et al*. 2000). In this work we configure a spring-mass-damper network for force feedback based on MRI tissue density measurements combined with data from in-vivo force measurements.

2. Theoretical model of reaction forces

During epidural needle insertion, the epiduralist encounters resistance to insertion which varies between the tissue layers. The resistance causes a reaction force opposite to the applied force. The total reaction force is felt by the anaesthetist during insertion, and so the haptic device needs to re-create the total reaction force to simulate the feeling of needle insertion.

A theoretical model was developed to partition reaction force into its constituents (Vaughan *et al.* 2013). The thumb applies force onto the plunger of the syringe and this force causes the saline to build up 'resultant pressure' in Eq. (1), see Fig. 1. Concurrently the other hand on the 'wings' guides and stabilises the Tuohy needle. The final driving force may solely be directed through the plunger since identifying 'loss of resistance' in epidural space is critical. The closed vessel causes a forward force on the needle. The tissue provides friction F_f, cutting resistance F_c and stiffness F_s, which combine into the reaction force F_r which is equal and opposite to the applied force in Eq. (2).

If the applied force becomes instantaneously greater than the reaction force the needle will move forwards, otherwise the needle remains stationary in relation to the tissue surface causing

tissue deformation.

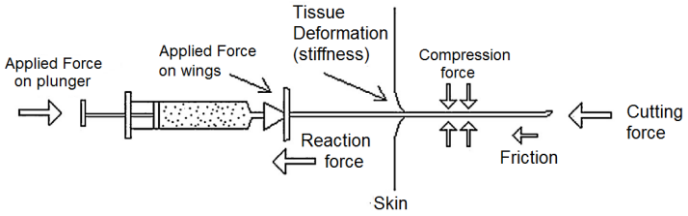

Fig. 1 Forces during needle insertion

$$P_r = (\frac{F_r}{A}) \tag{1}$$

where P_r is Resultant pressure of saline, F_r is thumb force on plunger, A is area of plunger.

$$F_r = F_c + F_f + F_s \tag{2}$$

where F_c is cutting force, F_f is due to friction and F_s contributed by stiffness of tissue.

Eqs. (1)-(2) are the basic relationship combining friction, stiffness and cutting force to calculate the reaction force for the haptic device to feedback.

The Novint Falcon was used for force feedback, which provides a three degrees-of-freedom (DOF) interface. Software implementations could additionally simulate insertions at various angles including paramedian and upward inclination angles (Carvalho 2008). Most desktop haptic devices exhibit some constraints such as the limit in their range of movement and force feedback range; the maximum force most can exert is around 15 N. Haptic devices need to deliver refresh rates of 300-1000 Hz (McNeely 2005) to provide realistic interaction.

A syringe was mounted onto the haptic device stylus to provide a familiar interface for epiduralists. The 3-DOF device provides ability to insert the needle along *Z* axis in the left handed Cartesian coordinate system but also the user can move the stylus in *X* and *Y* directions to choose the insertion site, shown in Fig. 2. Once the needle tip has entered the tissue, planar motions are not possible.

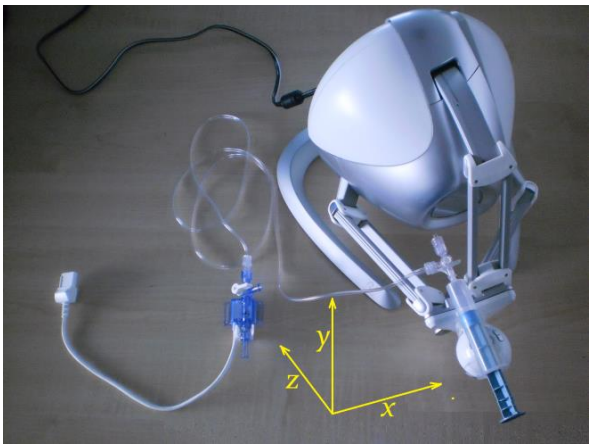

Fig. 2 Haptic device generating force along x, y and z axes

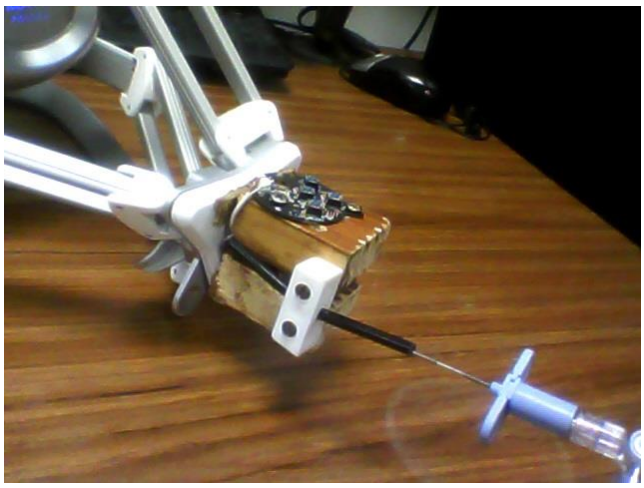

Fig. 3 Modified needle grip adapter for the Novint Falcon haptic device

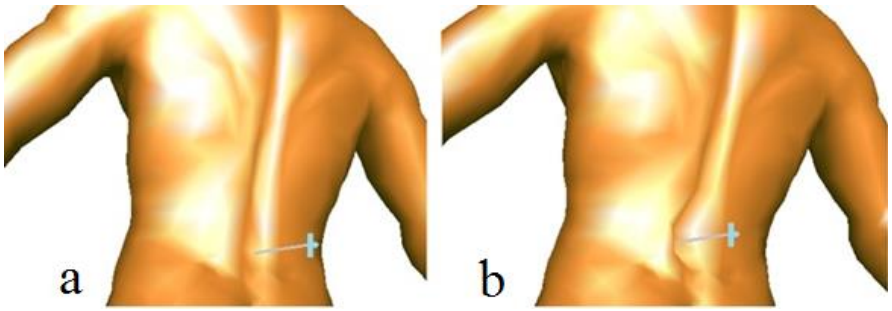

Fig. 4 (a) Initial patient torso (b) Needle insertion causes localised tissue deformation

The Novint Falcon was modified to allow the needle to connect onto the haptic device. This has the benefit that the force feedback can be experienced directly on the needle (Fig. 3). This was done using a frame to hold a metal tube into which the needle can be firmly held in place. The electronic circuit was mounted on top for access to buttons which run functions within the software.

A patient torso surface mesh was subjected to deformation from a needle, shown in before deformation in Fig. 4(a) and after deformation in Fig. 4(b). The extent of deformation was proportional to the differing position of the needle. The model provides an external view of the surface mesh. Spring-mass-damper could improve upon surface mesh deformation by also modelling the internal structure and density of tissues, allowing deformation to be felt externally as force feedback.

3. Spring-mass-damper model for haptic feedback

Spring-mass-damper was used to model the needle insertion deformation of internal tissue structures of various density. SMD has been shown to provide a realistic model for haptic tissue and medical simulations (Lebiedz *et al.* 2009), (Mollemans *et al.* 2003), (Picinbono *et al.* 2000), (Kuhnapfel *et al.* 2000), (Roose *et al.* 2012). There are other alternative techniques such as finite

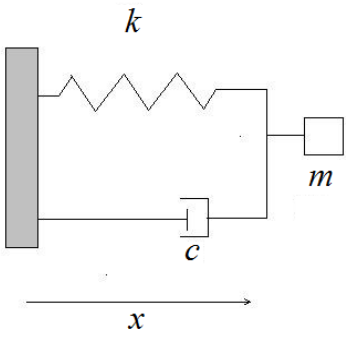

Fig. 5 Spring-mass-damper model of needle insertion

element, continuum mechanics (Delingette *et al*. 2004) chain mail (Gibson *et al.* 1997). Tissue deformation has had quite a lot of research interest and one of the most commonly researched tissues is skin (Picinbono *et al.* 2000).

Zhang *et al*. (2014) developed a haptic deformation model based on layered rhombus-chain. During the modeling, the accumulation of relative displacements in each chain structure unit in each layer is equal to the deformation on the virtual object surface, and the resultant force of corresponding springs is equivalent to the external force. Experimental study in non-homogenous virtual human liver and lungs provides stable and realistic haptic with vivid display.

The concept is of a mass connected to a spring combined with a damping element which resists motion, as shown in Fig. 5. This fits well with the case of needle insertion, the mass *m* represents applied force, the spring constant *k* represents tissue stiffness and the damping viscosity *c* represents tissue viscous properties. The shaded rectangle on the left represents the spine which remains stationary. As the mass overcomes the required force for each layer the needle moves forward.

When the needle has zero velocity and zero acceleration, the force exerted on the needle is registered by tissue elasticity given by Eq. (3). The stiffer the tissue (higher *k*), more force is required to cause deformation *x*. Once the applied force exceeds a critical value for each layer, the needle traverses the tissue. Tissue stiffness force is negative since as the needle is pushed toward the body, tissue elasticity counteracts by pushing away from the body.

$$F_s = -kx \tag{3}$$

where F_s is tissue reaction force, *k* is tissue stiffness, *x* is tissue deformation.

The damper represents tissue deformation with time. The effect of tissue damping is to slow down the motion of the needle. It produces a force opposite and proportional to velocity, shown in Eq. (4). Total force is found by combining stiffness and damping forces in Eq. (5).

$$F_d = -cv \tag{4}$$

where F_d is damping force, *v* is velocity of the mass, *c* is the damping viscosity.

$$F = F_s + F_d \tag{5}$$

where *F* is total reaction force.

Applied to the data for needle insertion, spring-mass-damper allows several benefits such as modelling the stiffness of tissue and the stiffness can vary along or during deformation.

4. Developed equation of damped oscillator for human tissue model

For modelling movement of deformable soft human tissue Eq. (6) was developed. The reason for developing this oscillation equation is to create an alternative method to the SMD method for tissue movement modelling and to produce comparable results to existing models such as Euler and Feynman algorithms (Volino *et al*. 1995). The advantage of an equation model is that it can directly calculate the oscillation properties at any time without need to sequentially progress through preceding time-steps as in an algorithmic solution. Also this could reduce or eliminate errors due to algorithmic ordering.

The developed model in Eq. (6) uses a damped harmonic oscillator. The model calculates displacement and velocity of oscillations over time by using exponentially decaying sinusoid model. The motion is diminished by viscous damping which is linearly dependent on velocity affected by Newton's second law. This type of motion represents a mass on a spring with damper, or a swinging pendulum with friction and air resistance for damping.

$$x = Ae^{-yt}cos(\omega_0 tp) \tag{6}$$

where:

x is displacement in meters (distance from rest position).
A is amplitude, initially set to 3.
y is damping coefficient, set to $\frac{c}{2m}$
t is time in seconds, from 0 to 25.
ω_0 is un-damped angular frequency, set to $\sqrt{\frac{k}{m}}$
p is the phase which determines sine wave starting point.
c is damping viscosity, set to 0.1.
m is mass set to 1kg.
k is Spring stiffness = 1N/m.
ω_1 is angular frequency, given by $\omega_0\sqrt{1-S^2}$
S is damping ratio which is $\frac{c}{2\sqrt{mk}}$

A comparison of various damping viscosities is shown in Fig. 6 based on Eq. (6) calculating displacement (x) over time (t). The amplitude (A) was set to 3m. Time was plotted in steps of 0.25 seconds from 0 to 25 seconds. The phase (p) represents the starting point of the sine wave which is set to 0 since the mass begins at rest. Spring stiffness (k) is taken as 1 N/m and mass (m) is 1 kg. The variables were initially fixed with these values to begin the oscillation. If values are adjusted this will affect the resulting output values. For modelling human tissues the values should closely resemble the properties of human tissue.

When spring strength is fixed in a damped system the oscillation frequency also becomes fixed to a set frequency, regardless of changes to damping viscosity (Fig. 6). Amplitude decreases towards zero over time dependent on viscosity. Viscous strength is conventionally classified into six categories: driven, un-damped, under-damped, damped, critically-damped and over-damped. In Fig. 6, viscosities 0.1 and 0.3 are under-damped. Viscosity 0.7 is over-damped which reduces amplitude more quickly in fewer oscillations. Viscosity 1.8 demonstrates a critically damped system which returns to steady state as quickly as possible without oscillating. Over-damped or highly over-damped oscillators return to equilibrium slower without oscillating. Driven oscillation

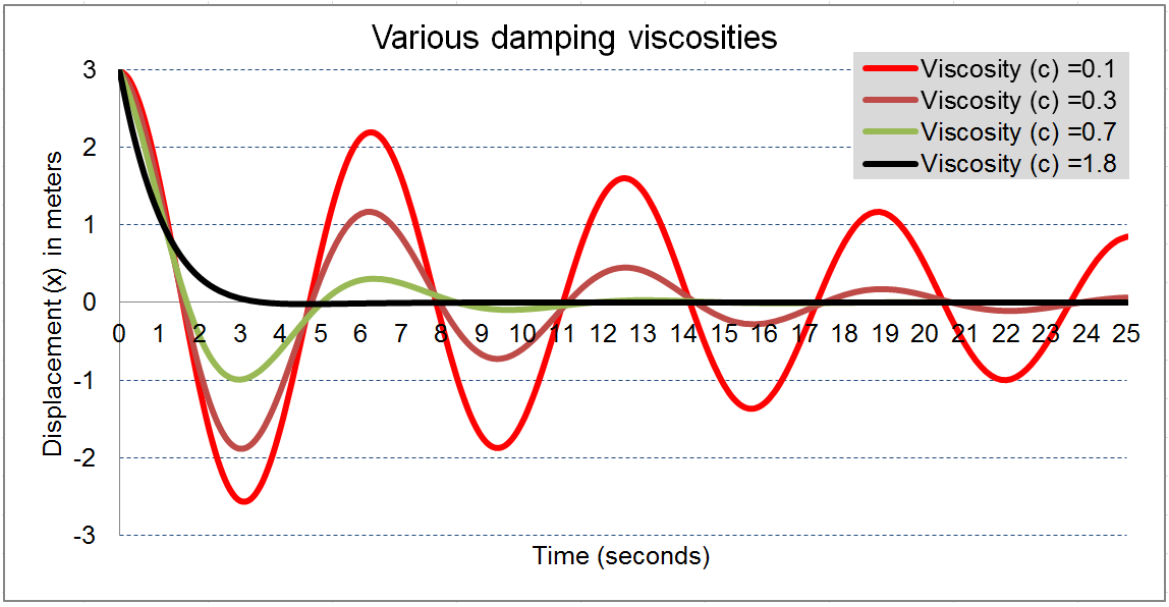

Fig. 6 Analytical calculation of various damped viscosities for simulation of biological tissues

systems gain energy over time. Un-damped systems have continuous amplitude without reducing over time. The viscosity system which most closely matches to human tissue may have viscosity between 1 and 1.4.

4.1 Comparison of developed tissue modelling equations to mathematical oscillation models

For performance assessment, results from developed model in Eq. (6) were compared to results from established oscillation algorithms. Three mathematical tissue displacement model algorithms were implemented; Euler, Euler-Cromer and Feynman-Newton (Volino *et al*. 1995). Others oscillation models are available, but these were used because they have become established stable oscillatory systems (Zhang *et al*. 2001).

Tests were conducted to identify which oscillator algorithm is the best fit to developed equation for motion of oscillations for tissue modelling. Analytical calculations were compared to results from each algorithm. For the three tested algorithms the representative equation and the implemented source code is shown in Table 1. The main difference between results from the three equations is caused by the time at which velocity is calculated with respect to each time-step.

Motion was modelled first with time-step h=0.25 seconds and then h=0.1 seconds to compare the results. Motion was plotted from 0 to 25 seconds during oscillation. Spring stiffness was k=1 N/m, viscosity c=0.1 kg/s.m and mass m=1 kg. Initial conditions for displacement x=1 m and velocity v=0 m/s.

In theory for a timestep h, Euler method has a truncation error proportional to h, while the Feynman method's truncation error is proportional to h^2. Thus, for a time-step of 0.1 the Feynman error is about one-tenth of the Euler error. So we could expect to find Euler method less accurate when compared to analytical solution.

Table 1 Equation and source code for each of the three implemented oscillation algorithms

	Euler	Euler-Cromer	Feynman
Equation	$x(t0+h)=x(t0)+h*v(t0)$	$x(t0+h)=x(t0)+h*v(t0+h)$	$x(t0+h)=x(t0)+h*v(t0+h/2)$
Algorithm in C++ programming language	a=-(k*xold+c*vold) v=vold+dt*a x=xold+dt*vold xold=x vold=v	a=-(k*xold+c*vold) v=vold+dt*a x=xold+dt*v xold=x vold=v	x=xold+dt*vold a=-(k*x+c*vold) v=vold+dt*a xold=x vold=v

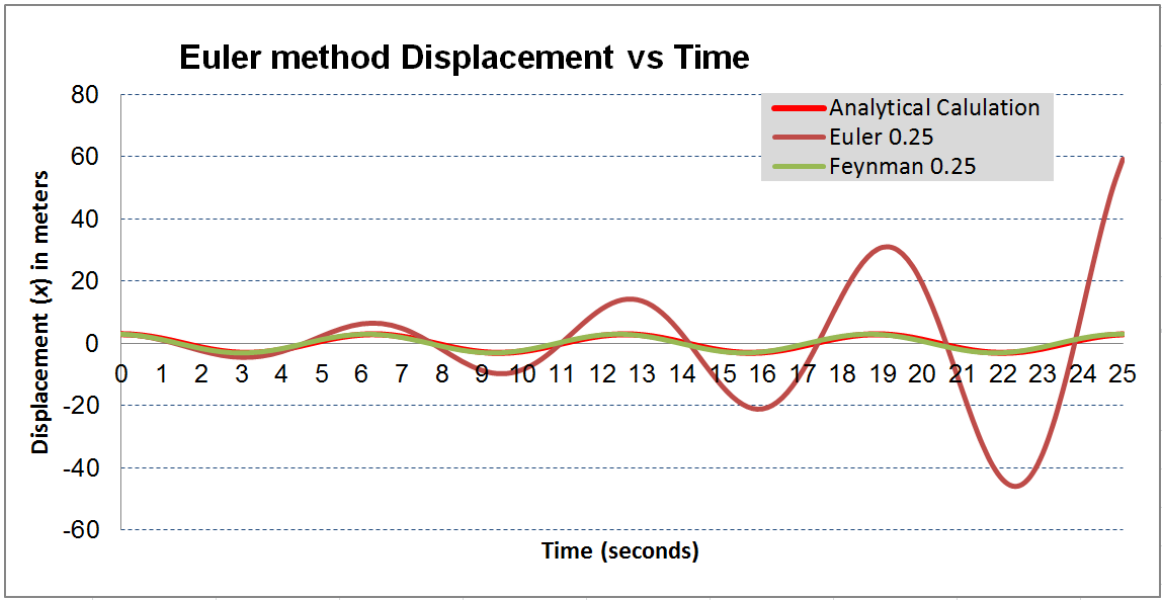

Fig. 7 Euler algorithm failed diverting exponentially away from the correct results

In order to assess the three algorithms, both displacement (x) vs time (t) and velocity (v) vs time were plotted. Additionally velocity vs displacement was plotted. The tests involved damped oscillation with a variety of different viscosities and stiffness.

4.2 Results of Euler algorithm assessment for soft tissue simulation

The Euler method did not correctly model either the un-damped or damped system. Results from Euler spring model exhibited characteristics of numerical instability. Exponential energy growth resulted in erroneous deviations from developed model (Fig. 7).

4.3 Results of Euler-Cromer algorithm assessment

The Euler-Cromer model produced relatively accurate results. Output was closer to the developed solution in Eq. (6) and was able to model curves at various stiffness and viscosities (Fig. 8.)

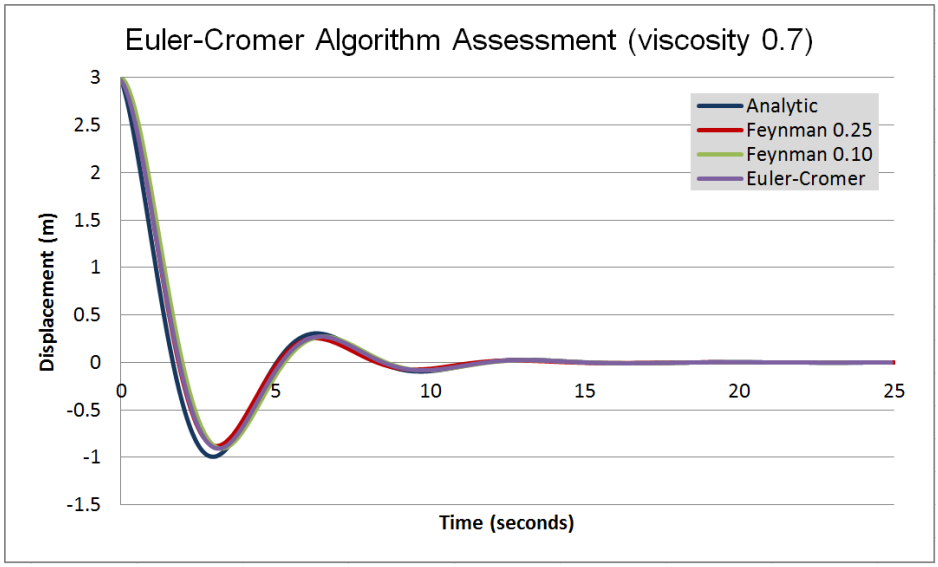

Fig. 8 Euler-Cromer models for tissue viscosity 0.7 measured with a 0.25 second timestep

4.4 Assessment of Feynman Algorithm for Soft Tissue Simulation

The basis for using Feynman method was the possibility to improve accuracy over classical method in (Timberlake 2008). The plots of Feynman gave the results most accurate to the developed equation model, following closely to the amplitude of the developed model, Eq. (6) on each phase (Fig. 9). The Feynman algorithm produced increased accuracy when the time-step was reduced from 0.25 to 0.10 seconds. However using a smaller time-step causes higher computational load.

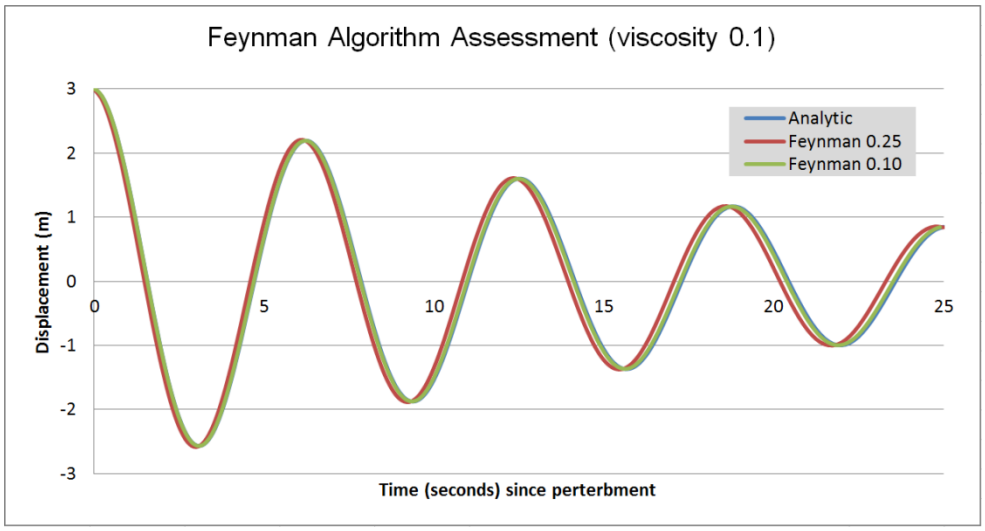

Fig. 9 Feynman Algorithm for 0.1 damping viscosity for relaxation of soft tissue simulation

4.5 Discussion of oscillation systems comparison

For un-damped oscillation the three tested algorithms Euler-Cromer and Feynman algorithm both successfully modelled the un-damped analytical equations well but Euler-Cromer was more out of step. This is because on the first iteration where time (t) is 0 the Euler-Cromer method adjusts the displacement whereas the Feynman retains initial displacement (x) at time 0, similar to the developed equation.

To analyse the displacement vs velocity during oscillations, phase plots were drawn for both Euler-Cromer and Feynman, which show the Euler-Cromer algorithm tends to displace mass earlier than Feynman algorithm. Fig. 10 demonstrates the relationship between the two methods, with viscosity of 0.1 and spring stiffness of 1 N/m.

Out of the three numerical algorithms, Euler, Euler-Cromer, and Feynman-Newton, the Feynman-Newton method best approximates results from the developed equation to both un-damped and damped oscillations which could model human tissue deformation. While a smaller time step for each method would help to better approximate the equation results, the Feynman-Newton method is the most efficient, because it does not require such a small time step, resulting in reduced computational load.

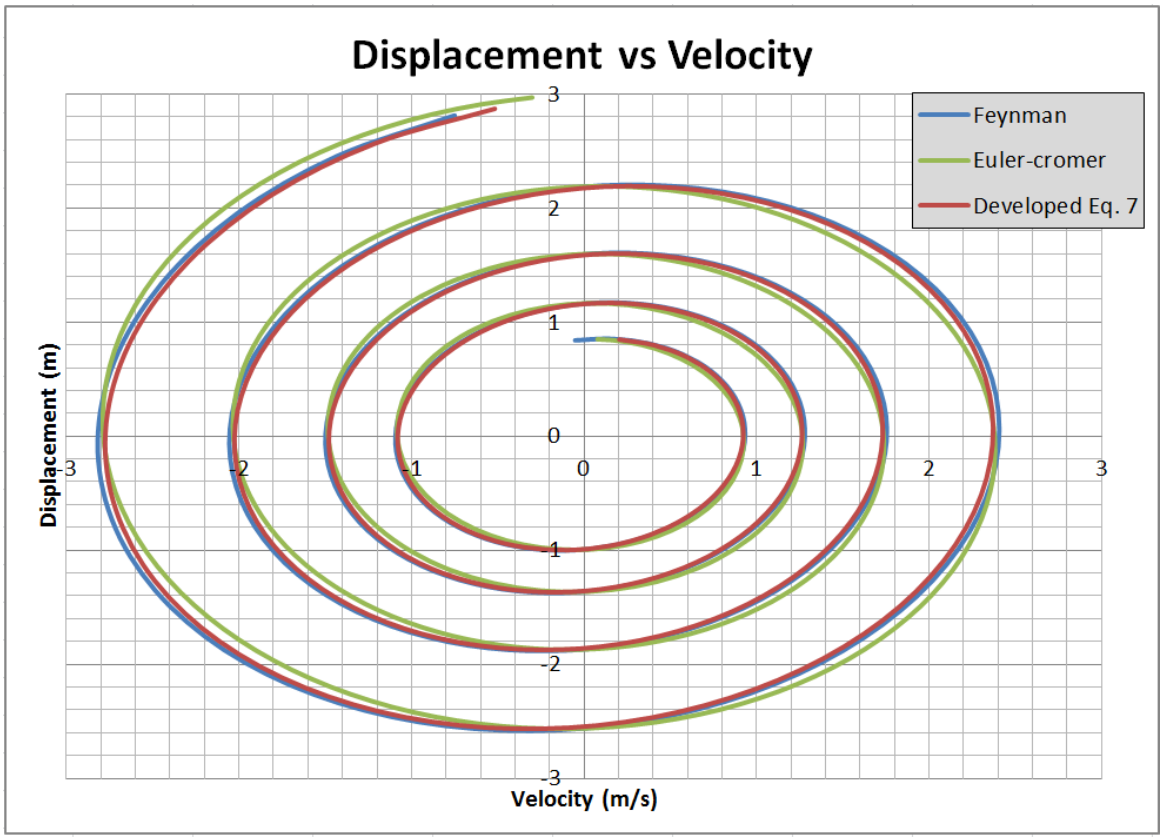

Fig. 10 Phase space plot for Euler-Cromer and Feynman with 0.1 viscosity and 0.1 time-step

5. Assembling networks of multiple SMDs

In order to connect many spring-mass-damper elements together in a 3D network, mathematical models were developed to implement assembly. Each node has a mass, position, velocity, acceleration and total force. Each spring has a stiffness, viscosity, initial length, velocity and connections to two nodes.

For each spring, current length is Euclidean distance between the two connected masses *m* and *n* in 3D space, Eq. (7). Displacement is the difference between spring's current length and initial length, Eq. (8). Spring's velocity is the change in spring's displacement over time, Eq. (9). The damper produces a force opposite and proportional to velocity, Eq. (10). Based on these, each spring's total force is calculated, Eq. (11).

$$L_s = \sqrt{(m_{xc} - n_{xc})^2 + \left(m_{yc} - n_{yc}\right)^2 + (m_{zc} - n_{zc})^2} \tag{7}$$

where L_s is spring length, *m* and *n* are two interconnected mass positions and *xc*, *yc*, *zc* are the Cartesian coordinates of the masses.

$$x = L_{s2} - L_{s1} \tag{8}$$

where *x* is spring displacement, L_{s1} is initial spring length and L_{s2} is current spring length.

$$v = \frac{x_2 - x_1}{t_e} \tag{9}$$

where *v* is spring velocity, x_1 is previous spring displacement, x_2 is current spring displacement and t_e is elapsed time since previous iteration.

$$F_d = Cv \tag{10}$$

where F_d is damping force and *C* is damping viscosity.

$$F = Kx - Cv \tag{11}$$

where *F* is total spring force and *K* is spring stiffness

Total spring force affects both connected nodes equally, so to achieve this we need to apply each springs force onto the two interconnected nodes *n* and *m* by assigning a force vector along the 3D direction of the spring by calculating proportion of *x*, *y* and *z* separately, Eq. (12) and the force on node *n* is the opposite of node *m*, Eq. (13). The total force on each node can then be found by summing all forces from each spring connected to it, Eq. (14). The total force causes the node to accelerate, Eq. (15). The acceleration of a node is added to its current velocity, Eq. (16). The velocity is added to its current position, Eq. (17). The adjusted positions affect lengths of surrounding springs, starting the process again, causing a cycle of force distribution through the SMD network. Nodes connected to bone or under needle tip are given very high mass, so that they accelerate and move much less. Haptic force feedback felt by the user is equal to total force on the node under needle tip.

$$\begin{aligned} F_{m_x} &= F(m_{xc} - n_{xc}) \\ F_{m_y} &= F\left(m_{yc} - n_{yc}\right) \\ F_{m_z} &= F(m_{zc} - n_{zc}) \end{aligned} \tag{12}$$

where *n* and *m* are two interconnected nodes, F_m is force vector in node *m* and *F* is total spring force.

$$F_n = -F_m \tag{13}$$

where F_n is force vector in node n and F_m is force vector in node m.

$$F_{tm} = \sum_{i=1}^{n} \frac{F_i}{2} \tag{14}$$

where F_{tm} is total force on node m, F_i is total spring force of spring i and n is the number of springs connected to the mass.

$$A_m = F_{tm}/M_m \tag{15}$$

where A_m is acceleration of node m and M_m is the mass of node m.

$$V_m = t_e\, A_m + V_{pm} \tag{16}$$

where V_m is velocity of node m, t_e is elapsed time since previous iteration, V_{pm} is previous velocity of node m at time $(t_c - t_e)$ and t_c is current time.

$$P_m = t_e\, V_m + P_{pm} \tag{17}$$

where P_m is new position of node m and P_{pm} is previous position of node m at time $(t_c - t_e)$.

Eqs. (7)-(17) were formed into a function using C programming language. Below is the resulting pseudo-code algorithm that was developed using the equations, which produces the 3D implementation of human tissue deformation with oscillations. The output of this can be seen in Fig. 11 where the circular nodes are moving during deformation and the lines represent the direction of total force on each node, calculated as the sum of all spring forces.

```
for each spring{
  distance = nodeA – nodeB;
  displacement=distance-initialdistance;
  springvelocity=(displacement-olddisplacement)/timestep;
  springforce = stiffness*displacement-viscocity*velocity;
  nodeA.force+=springforce/2;
  nodeB.force-=springforce/2;}
for each node{
  accelleration = totalforce/mass;
  velocity += acceleration;
  currentposition += velocity;}
```

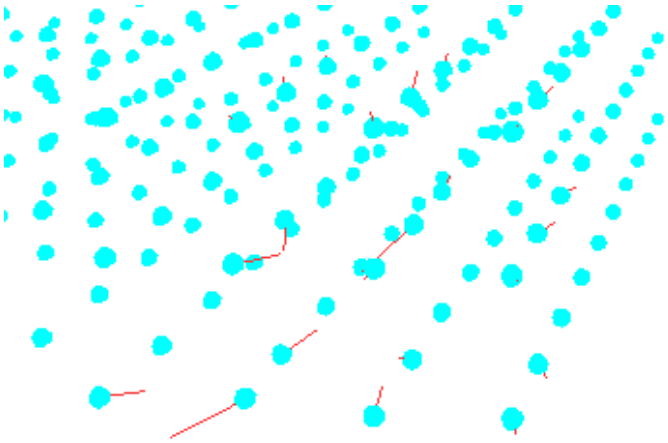

Fig. 11 The lines indicate direction of total force on node matrix during a tissue deformation

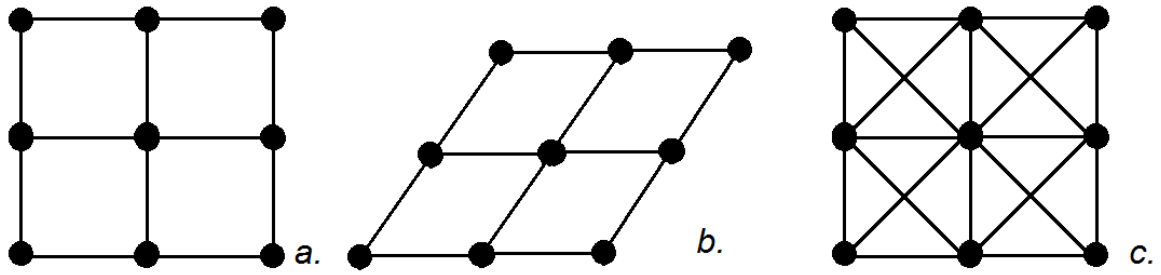

Fig. 12 Higher number of spring connectivity produces more realistic tissue simulation

The number of spring connections between the masses was chosen due to the problem shown in Fig. 12. With lower connectivity shown in Fig 12(a), the simulated tissue can be skewed in certain ways such as in Fig. 12(b) without affecting the length of any springs. In this case, the tissue will not return to its original shape. In this model higher connectivity is used, shown in Fig. 12(c), so that any stretching or skewing of the simulated tissue will affect spring lengths causing the tissue to exhibit elastic characteristics. Resulting volumetric structures contain over twice the number of springs which increases computation but real time simulation remains achievable.

Various other methods have been proposed to show the behaviour of a spring-mass-damper system such as by solving differential equations or standard analytical methods. With a large number of nodes, generally numerical methods become necessary. Some proposed solutions include Euler's method, Verlet integration or Fourth order Runge-Kutta method (Eriksson 2013).

5.1 Creating 3D network of SMDs representing tissues

A graphical representation of tissue was created for the epidural simulator so that the haptic device could work in parallel with the visual feedback. A block of simulated tissue was created using a 3D grid of spring-mass-damper assemblies. The cube has ten nodes on each side, shown in Fig. 13. As the needle advances through the tissue layers, the springs are compressed and reaction force is calculated and generated as haptic feedback.

Using a point cloud to store all masses enables each node to contain a 3D location plus intensity representing the mass at that node. Medical imaging often makes use of point clouds to represent volumetric data and achieve multi-sampling and data compression (Sitek *et al.* 2006). Surface reconstruction from a point cloud is possible by converting into polygon or triangle mesh models, NURBS surface models, or CAD models. Several open source libraries for managing point clouds are available (Koutsoudis *et al.* 2013) including MeshLab, CloudCompare and Point Cloud Library (PCL).

The block of tissue was adapted to contain seven layers of various thickness, stiffness and density, shown in Fig. 14 for epidural insertion. The layers represent the tissues and ligaments experienced during an epidural needle insertion.

The haptic device stylus is displayed as a needle. A surface mesh human torso was added with adjustable transparency to give the option of internal or external view. Additionally a cross section view shows tissue deformation along the sagittal plane of the torso. Real-time feedback is provided from the simulator as text on screen showing the applied force. Applied force is calculated from continuous measurements of the saline pressure using a pressure transducer

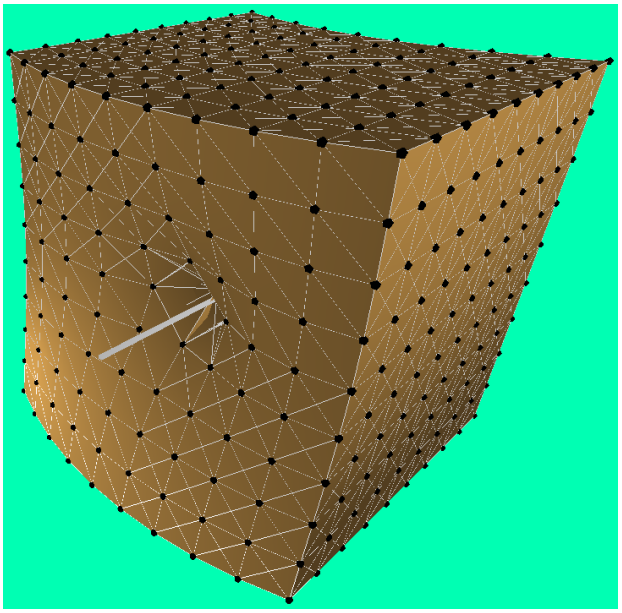

Fig. 13 Network of multiple spring-mass-damper models simulating tissue deformation

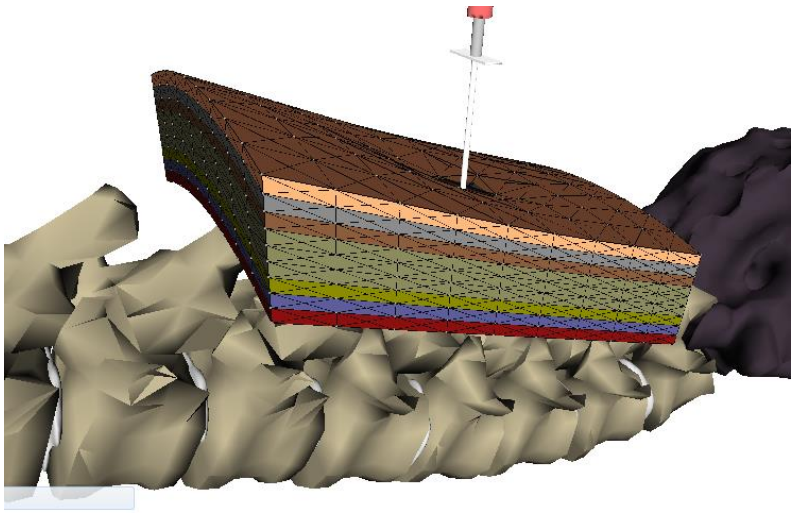

Fig. 14 Simulated tissue layers with deformation under the needle

(Vaughan *et al*. 2013). An alternative method to calculate applied force could be by the displacement of the haptic stylus caused by external applied force. The graphics runs at around 31 FPS whilst displaying the full array of 1000 masses with interconnected springs. However the haptic device still retains its speed because the servo motors run at 1000 Hz giving seamless haptic feedback.

When a force is applied by the user the software gives estimates for friction, stiffness and cutting force, based on the theoretical model. Each layer has a defined cutting force and if the calculated proportion of applied force exceeds that limit, the haptic device allows the needle to

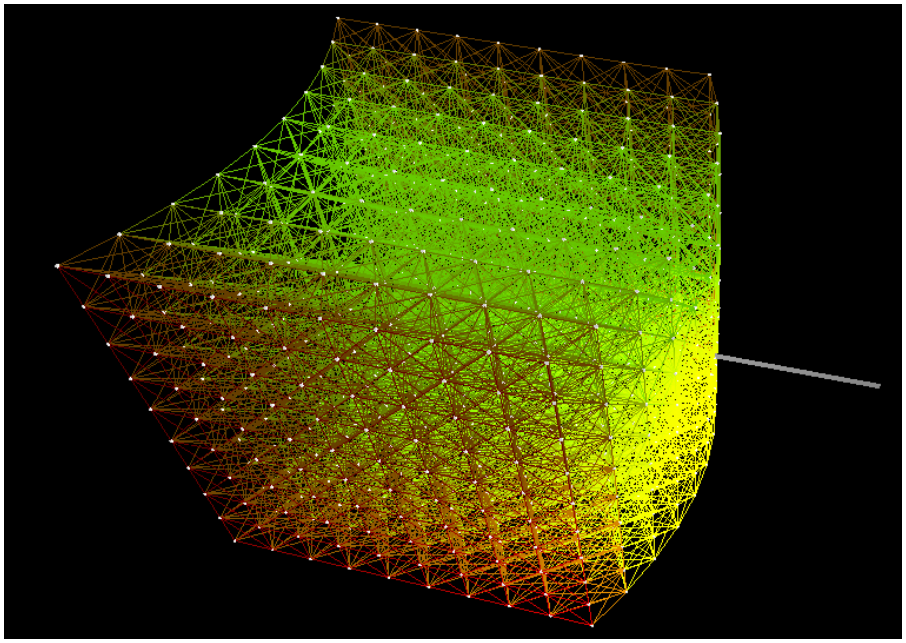

Fig. 15 Heterogenous stiffness modelling for tissue structures

slowly move deeper. Force from the user is applied onto the spring-mass-damper network at the point of needle contact allowing the SMD to calculate tissue displacement caused on each mass and the force from each spring.

This layer based setup may be a satisfactory representation of the shape of skin and fat layers. Heterogenous distribution of stiffness and density allows an accurate depiction of tissue structure in-vivo. The spring-mass-damper network in Fig. 15 demonstrates variation in a three dimensional tissue structure. The varying colour of the springs indicates varying spring stiffness. The mass of each node also varies throughout the object.

6. Palpation and using ultrasound probe

Palpation of the patient's back is the process whereby the epiduralist locates landmarks to choose the optimal needle insertion site. Recently ultrasound is becoming increasingly used to measure depth of epidural space and monitor epidural needle advancement towards the target (Carvalho 2008). A comprehensive simulation should also train these important skills. Simulation of palpation (Fig. 16) and ultrasound probe movement on the skin (Fig. 17) is also possible using SMD layers and was implemented in the needle insertion simulator. These both interact with the tissue surface in a similar way to the needle except they cannot cut through tissue, so there is no cutting force or friction. Reaction force in this case is comprised solely of tissue stiffness, which is calculated according to displacement of the SMD masses proportional to applied force onto the skin surface.

During palpation, bony landmarks are felt through the skin as a rigid body from the surface, allowing the user to choose an appropriate needle insertion location. Palpation requires experience

and haptic simulation can help develop this skill. Palpation is an important part of the training for epidural insertions. The applied force from palpation is distributed onto the SMD over a surface area of the finger tip. Basic palpation is implemented with a hand which can move and apply forces. The hand movement is controlled from the haptic device with force feedback calculated from SMD. To further improve accuracy forces could be measured in-vivo during palpation.

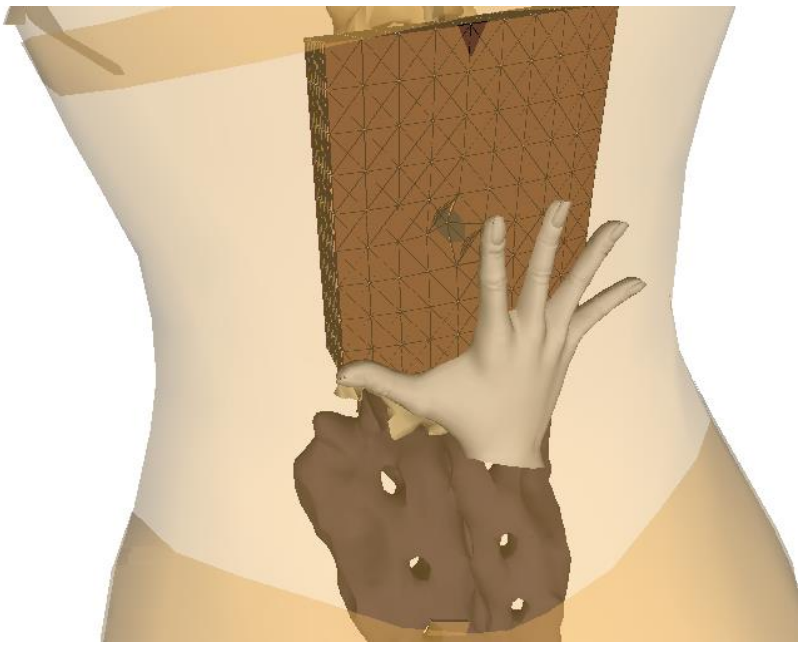

Fig. 16 Palpation simulation with tissue deformation

Fig. 17 Skin deformation under ultrasound probe

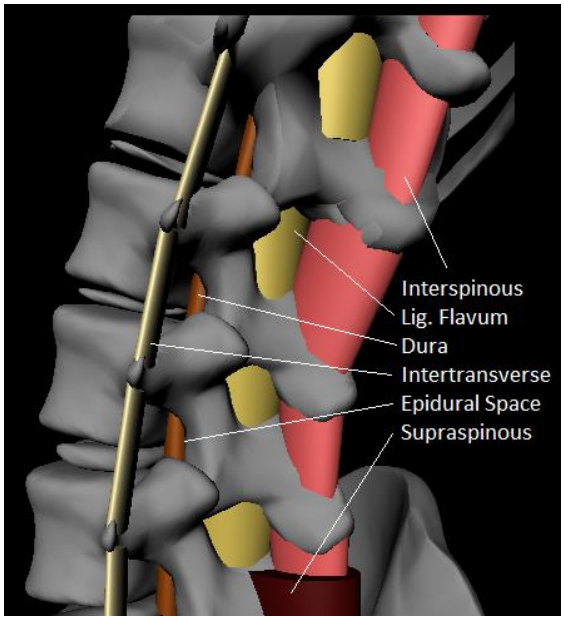

Fig. 18 Surface mesh model of ligaments

7. Voxelization of surface mesh

To model the correct geometrical shape of the spinal ligaments and vertebrae, a surface mesh was created as shown in Fig. 18. Ligamentum flava are C-shaped tough ligaments connected between vertebrae near the internal wall surrounding the dura and epidural space. This mesh provides correct geometry for each ligament and bone in the anatomy.

Surface mesh can describe the geometrical shape of each ligament more accurately. However it lacks internal structure which is required to model the force feedback and deformation with spring-mass-damper. To solve this issue, a method was implemented using voxelization to fill the interior of the surface mesh with voxels (Pasko *et al*. 2008) (Huang *et al*. 1998). The advantage is that voxels define the positions for a distribution of mass and spring stiffness to be defined throughout the object, matching the exterior shape of any surface mesh.

The voxelization method is initiated by creating a voxel at the central point of the mesh between external boundaries. The 26 neighboring voxels are created forming a cube, if they are inside the mesh edge. Mesh edge is detected when surface mesh points are inside the voxel cube. For each new voxel, the process is repeated. This is achieved with bounding box around each voxel to create a voxel grid. The aggregate result of all voxels is a tessellation of 3D Euclidean space, which avoids inaccurate artefacts appearing in corners. Voxels cannot overlap so algorithmic checks to ensure only one voxel is created at each point, although many of the 26 neighbouring voxels share a vertex, edge or face with their neighbour. The center voxel shares edges with twelve neighbours, shares a vertex with eight neighbours and shares a face with six neighbours. The result is neighbourhood space being filled close to all edges of the polygonal mesh.

This method enables voxels to fill around corners. Voxel size was set small enough to fill narrow spaces. Ligamentum flavum surface mesh is shown in Fig. 19(a) after the internal volume

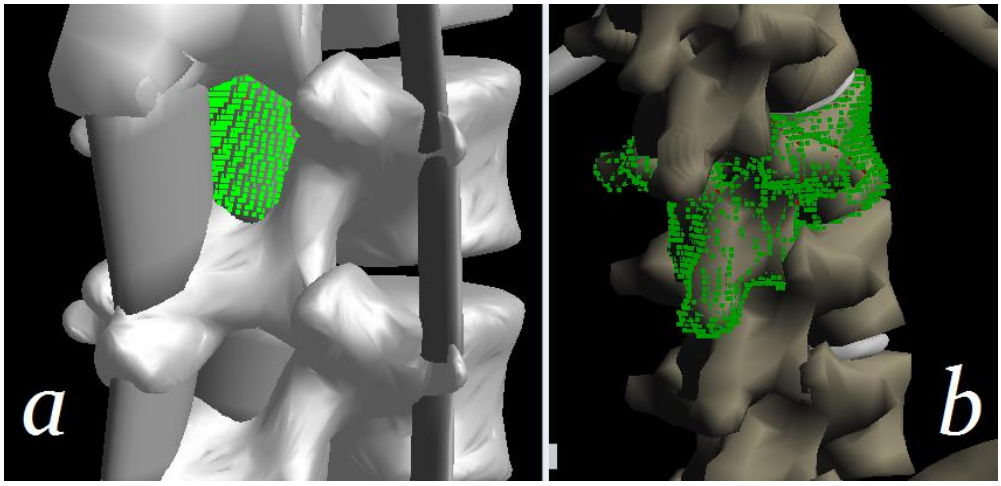

Fig. 19 Voxelization of surface mesh (a) Ligamentum flavum. (b) Vertebra

was filled with voxels. Alternative voxelization processes for surface meshes have been defined by Lee *et al*. (2012) and Huang *et al*. (1998).

Once voxelized, each of the coordinates from each voxel was used as one of the nodes to construct a spring-mass-damper assembly. Fig. 19(b) shows parts of the ligament and bone surface mesh. These parts were filled with voxels and then converted into a spring-mass-damper network to allow force feedback needle insertion and deformation.

8. Tissue stiffness modelling using MRI

The aim of MRI stiffness modelling is to read tissue stiffness from MRI images so that actual patient data can be modelled on a SMD network for force feedback. Patient lumbar MRI scans were obtained from various patients as part of our on-going clinical trial (Vaughan *et al*. 2012, 2013). These MRI are used to provide a graphical depiction of internal tissue density distribution. These were used to configure the spring-mass-damper network with varying stiffness, dependent on the brightness throughout each MRI image. On the MRI setup, spacing between slices is set to 1.25 mm as shown in Fig. 20.

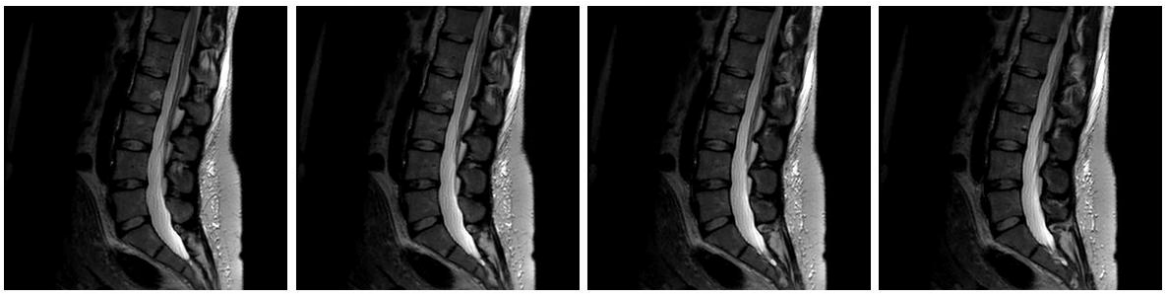

Fig. 20 MRI image intensity used to configure SMD tissue density distribution

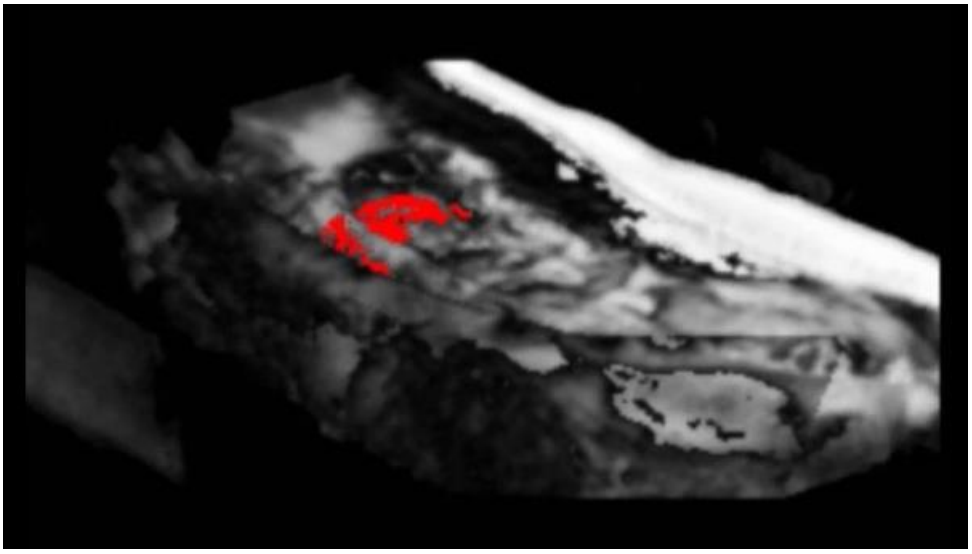

Fig. 21 Patient MRI slices combined into 3D volume with soft and hard tissues

The SMD network is set up with 1.25 mm between layers to match MRI thickness. MRI provides a good contrast between the different soft tissues of the body, because the atomic nuclei of each tissue type respond to and align to the magnetization differently. With T_1-weighted MRI, fat-containing tissues are bright and fluid-containing tissues are dark, and with T_2-weighted MRI vice-versa. This data for the fluid contents of various areas can indicate the stiffness which can be used to directly configure the spring stiffness throughout the SMD network.

A method was developed for using patient MRI data to configure the tissue stiffness on the spring-mass-damper assemblies. The process involves combining each separate MRI slice into a single 3D volume, shown in Fig. 21. A spring-mass-damper network is defined in memory, with enough nodes and springs to hold all sample data from all MRI slices in a single 3D volume, where *X* and *Y* are samples from individual images and *Z* is the number of slices, which is equal to total MRI scan depth divided by the MRI slice spacing. A loop processes the first MRI image incrementing from left to right then top to bottom. At each node the mean illumination of the surrounding 9 pixels is taken. This measurement is from 0 to 1 representing black to white on the MRI image. A second loop sets each spring's stiffness to equal the mean MRI intensity at the two nodes locations between which each spring is connected.

An additional use for the MRI is to accurately measure each patient's tissue layer thickness enabling modelled thickness to match the real tissues.

9. Measured patient data configured into the haptic device

Patient data for epidural insertion was obtained by conducting a clinical trial to measure the saline pressure during epidural needle insertion. The methods for recording epidural pressures during insertion used an in-house developed custom wireless pressure transducer and transmission system. A wireless receiver was placed in the hospital to receive clinical trial data from patients of various BMI. The sterile devices were initially developed as part of previous work (Vaughan *et al*.

2013) and were tested on a porcine model, prior to in-vivo application.

Measured pressure data from patients in our clinical trial was then programmed into the haptic device. The clinical trial produced graphs of saline pressure during insertion for patients with various BMIs. Data incorporation was done by setting the SMD tissue stiffness in each layer to match measured data. The result in simulation is that when applied force on the haptic device exceeds the required force for the current layer, the needle is allowed to pierce deeper. Configuring the haptic device with measured patient data has several benefits. (i) Simulated forces are verified to be accurate. (ii) The SMD network can be configured with values from various BMI patients to simulate obesity. (iii) Data provides an analysis testing benchmark, allowing comparison of applied force during simulation to measured saline pressure during simulation, and the saline pressure measured from in-vivo procedures.

9.1 Comparison between haptic feedback forces and pressure

During a simulated needle insertion on the spring-mass-damper layer based tissue structure, a graph was generated from the haptic software to plot the applied force, measured by saline pressure, in conjunction with haptic reaction force for a comparison (Fig. 22). Applied force was measured as saline pressure multiplied by the area of plunger from a pressure transducer. The needle depth was also plotted which was achieved by video processing to detect the visible needle using a camera (Vaughan *et al*. 2013). The shape of the applied force graph is similar to the haptic reaction force. Applied force occasionally is the greater of the two, which is when the needle pierces through. The resulting pressure graphs during simulation exhibit similar characteristics to the shape of graphs recorded in-vivo during patient procedures.

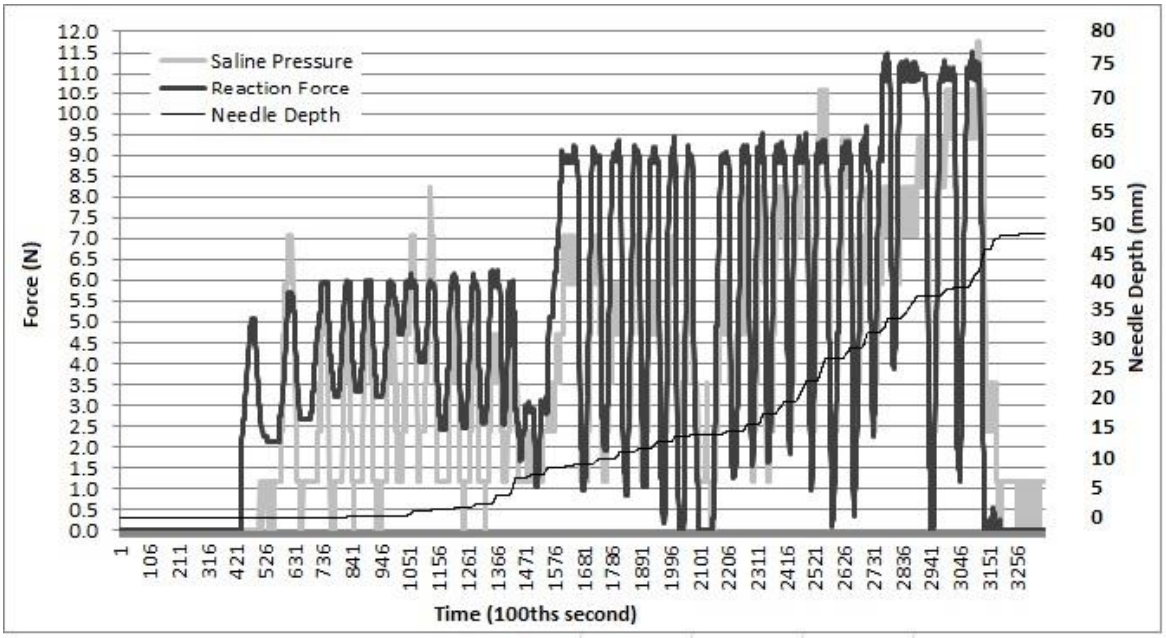

Fig. 22 Comparison of saline pressure and reaction force during simulated intermittent technique

Force feedback graphs were generated from the haptic device to compare the applied force to the haptic reaction force. It can be seen in Fig. 22 that reaction force generally follows the applied force.

A commercially available Novint Falcon haptic device was used. The device has large enough range of motion to encompass full movement of simulated needle. Three degrees of freedom allow the needle to move to various thoracic insertion levels centered on L3/L4. Haptic baud rate is controlled by hardware at 1000 Hz which results in fast seamless force adjustments. The frame-rate of the graphical simulator virtual reality interface was running at 60 frames per second. The pressure measuring device was sending wireless data at baud rate of 9600 with 8 data bits and no parity bit. Software to receive data was running as a separate thread from the graphics which eradicated delays. Development is planned for a custom built haptic device specifically for epidural needle insertion.

10. Conclusions

Three methods were presented for generating haptic feedback during needle insertion into tissues of various densities. The first method uses a curved grid of spring-mass-damper assemblies which is divided into several layers, each with various thickness and density. The second method used voxelization of a surface mesh to generate spring-mass-damper assemblies which geometrically match shapes of ligament or bones. The third method uses MRI to read actual patient tissue stiffness, combining all slices into a 3D volume to allow haptic feedback from patient MRI data.

Spring-mass-damper has proven to be a useful model to achieve real time tissue deformation and calculation of haptic reaction forces from simulated needle insertion. Volumetric data from MRI was used to assign the tissue density and mass distribution onto a SMD modelled tissue object.

Ultrasound images are also being collected as part of the trial, and could provide similar information about the tissue density. Ultrasound is the most commonly used procedure in epidural administration for estimating epidural space depth. The brightest areas in US images represent the strongest sound wave echo, which could determine the density of tissue regions. However ultrasound does not provide a 3D depiction making it harder to determine the exact location of the plane being viewed.

Analysis of algorithmic methods for oscillation were compared to new developed equations for modelling human tissue which resulted in identification of the most accurate results between algorithmic solutions and developed equation models.

Patient data from a clinical trial with various BMI obstetric patients has provided accurate syringe saline pressure measurements during epidural procedures. This has been incorporated into the haptic device by adjusting the stiffness of the various simulated tissue layers. The resulting accuracy was assessed by plotting graphs of applied force and haptic reaction force, which can provide comparison to the measured clinical data.

Overall the improved accuracy of haptic force feedback for simulated epidural procedures will improve the training for anaesthetists. The overall aim is to result in decreased risk of injury to patients and this will save money for the National Health Service (NHS) on costs of insurance claims for accidental injuries.

Acknowledgment

The research described in this paper was financially supported by Poole Hospital NHS Foundation Trust and Bournemouth University. MRI patient data was obtained with a clinical trial grant from Obstetric Anaesthetists Association. Kimal plc provided sterile transducer kits which were used during the clinical trial.

References

Agus, M., Giachetti, A., Gobbetti, E., Zanetti G. and Zorcolo, A. (2003), "Real-time haptic and visual simulation of bone dissection", *Presence: Teleoper. Virtual Environ.*, **12**(4), 110-122.

Carvalho, J.C.A. (2008), "Ultrasound-facilitated epidurals and spinals in obstetrics", *Anesthesiol. Clin.*, **26**(1), 145-158.

Delingette, H. and Ayache, N. (2004), "Soft tissue modelling for surgery simulation", *Handbook Numer. Anal.*, **12**, 453-550.

DiMaio, S.P. and Salcudean, S.E. (2002), "Simulated interactive needle insertion", *In 10th Symposium on Haptic Interfaces for Virtual Environ. Teleoper. Sys.*, 344–351.

Eriksson, E. (2013), "Simulation of biological tissue using mass-spring-damper models", Doctoral dissertation, Ö rebro University.

Gibson, S., Samosky, J., Mor, A., Fyock, C., Grimson, E., Kanade, T., Kikinis, R., Lauer, H. and McKenzie, N. (1997), "Simulating arthroscopic knee surgery using volumetric object representations, real-time volume rendering and haptic feedback", Eds. Troccaz, E. Grimson, and R. Mosges, *Proceedings of the First Joint Conference CVRMed-MRCAS'97, Lecture Notes in Computer Science*, Springer Berlin Heidelberg.

Huang, J., Yagel, R., Filippov, V. and Kurzion, Y. (1998), "An accurate method for voxelizing polygon meshes", *IEEE Symposium on Volume Visualization*, 119-126.

Koutsoudis, A., Vidmar, B., Ioannakis, G., Arnaoutoglou, F., Pavlidis, G. and Chamzas, C. (2013), "Multi-image 3D reconstruction data evaluation", *J. Cult. Herit.*, **15**(1), 73-79.

Kruse, S.A., Smith, J.A., Lawrence, A.J., Dresner, M.A., Manduca, A.J.F.G., Greenleaf, J.F. and Ehman, R.L. (2000), "Tissue characterization using magnetic resonance elastography: preliminary results", *Phys. Med. Boiol.*, **45**(6), 1579.

Kuhnapfel, U., Akmak, H. and Maa, H. (2000), "Endoscopic surgery training using virtual reality and deformable tissue simulation", *Comput. Graphic.*, **24**(5), 671-682.

Lebiedz, J., Skokowski, J. and Flisikowski, P. (2012), "Modelling of human tissue for medical purposes", *J. Med. Inform. Technol.*, **21**, 1642-6037.

Li, B., Li, X., Wang, K., and Qin, H. (2012) "Surface mesh to volumetric spline conversion with generalized poly-cubes," *IEEE Transactions on Visualization and Computer Graphics*, IEEE computer Society Digital Library.

Manoharan, V., van Gerwen, D., van den Dobbelsteen, J.J. and Dankelman, J. (2012), "Design and validation of an epidural needle insertion simulator with haptic feedback for training resident anaesthesiologists", *IEEE Haptics Sympos.*, 341-348.

McNeely, W.A., Puterbaugh, K.D. and Troy, J.J. (2005), "Six degree-of-freedom haptic rendering using voxel sampling", *ACM SIGGRAPH Courses*, **42**.

Mollemans, W., Schutyser, F., Van Cleynenbreugel, J. and Suetens, P. (2003), *Tetrahedral mass spring model for fast soft tissue deformation, In Surgery Simulation and Soft Tissue Modeling IS4TM*, Springer, Berlin, Heidelberg.

Okamura, A.M., Simone, S. and O'Leary, M.D. (2004), "Force modeling for needle insertion into soft tissue", *Biomed. Eng.*, **51**(10), 1707-1716.

Panait, L., Akkary, E., Bell, R.L., Roberts, K.E., Dudrick, S.J. and Duffy, A.J. (2009), "The role of haptic

feedback in laparoscopic simulation training", *J. Surg. Res.*, **156**(2), 312.
Pasko, A., Adzhiev, V., and Comninos, P. (2008), "Heterogeneous objects modelling and applications: collection of papers on foundations and practice", Springer, 4889.
Picinbono, G., Lombardo, J.C., Delingette, H. and Ayache, N. (2000), "Anisotropic elasticity and forces extrapolation to improve realism of surgery simulation", *ICRA2000: IEEE International Conference Robotics and Automation*, 596-602.
Roose, L., De Maerteleire, W., Mollemans, W. and Suetens, P. (2005), "Validation of different soft tissue simulation methods for breast augmentation", *Proceedings of the 19th International Congress and Exhibition (CARS Computer Assisted Radiology and Surgery)*, *Elsevier International Congress Series*, **1281**, 485-490.
Sitek, A., Huesman, R.H. and Gullberg, G.T. (2006), "Tomographic reconstruction using an adaptive tetrahedral mesh defined by a point cloud", *IEEE Trans. Med. Imag.*, **25**(9), 1172-1179.
Timberlake, T. and Hasbun, J.E. (2008), "Computation in classical mechanics", *Am. J. Phys.*, **76**(4), 334-339.
Vaughan, N., Dubey, V.N., Wee, M. and Isaacs, R. (2012), "Measuring tuohy needle insertion force on a porcine spine", *6th International Conference on Bioinformatics and Biomedical Engineering*.
Vaughan, N., Dubey, V.N., Wee, M.Y. and Isaacs, R. (2013), "Towards a realistic in vitro experience of epidural Tuohy needle insertion", *Proceedings of the Institution of Mechanical Engineers, Part H: J. Eng. Med.*, **227**(7), 767-777.
Volino, P., Courchesne, M. and Magnenat Thalmann, N. (1995), "Versatile and efficient techniques for simulating cloth and other deformable objects", *In Proceedings of the 22nd annual conference on Computer graphics and interactive techniques*, ACM.
Zhang, X., Sun, W. and Song, A. (2014), "Layered rhombus-chain-connected model for real-time haptic rendering", *Artific. Intell. Rev.*, **41**(1), 49-65.
Zhang, Y., Prakash, E. C. and Sung, E. (2001), "Real-time physically-based facial expression animation using mass-spring system", *Computer Graphics International* 2001, *IEEE Proceedings*, 347-350.

CC